Aftershocks driven by a high-pressure CO_2 source at depth

Stephen A. Miller[1], Cristiano Collettini[2], Lauro Chiaraluce[3], Massimo Cocco[3], Massimiliano Barchi[2] & Boris J. P. Kaus[4]

[1]*Institute of Geophysics, Swiss Federal Institute of Technology (ETH), 8093 Zürich, Switzerland*
[2]*Università degli Studi di Perugia, Perugia, 06100 Italy*
[3]*Instituto Nazionale di Geofisica e Vulcanologia, Rome, 00143 Italy*
[4]*Geology Institute, Swiss Federal Institute of Technology (ETH), 8092 Zürich, Switzerland*

In northern Italy in 1997, two earthquakes of magnitudes 5.7 and 6 (separated by nine hours) marked the beginning of a sequence that lasted more than 30 days, with thousands of aftershocks including four additional events with magnitudes between 5 and 6. This normal-faulting sequence is not well explained with models of elastic stress transfer[1,2], particularly the persistence of hanging-wall seismicity[3] that included two events with magnitudes greater than 5. Here we show that this sequence may have been driven by a fluid pressure pulse generated from the coseismic release of a known deep source[4] of trapped high-pressure carbon dioxide (CO_2). We find a strong correlation between the high-pressure front and the aftershock hypocentres over a two-week period, using precise hypocentre locations[5] and a simple model of nonlinear diffusion. The triggering amplitude (10–20 MPa) of the pressure pulse overwhelms the typical (0.1–0.2 MPa) range from stress changes in the usual stress triggering models[1,6]. We propose that aftershocks of large earthquakes in such geologic environments may be driven by the coseismic release of trapped, high-pressure fluids propagating through damaged zones created by the mainshock. This may provide a link between earthquakes, aftershocks, crust/mantle degassing and earthquake-triggered large-scale fluid flow.

The 1997 Umbria–Marche seismic sequence in the Northern Apennines, Italy (Fig. 1a), occurred on shallow-dipping (~40°) normal faults, migrating from north-northwest (NNW) to south-southeast (SSE) along an area of about 40 km in length and 15 km in width. Structural geology studies showed that the earthquakes nucleated close to the deeper portion of a thrust, and that the faults were not optimally oriented relative to the regional stress field[7]. Non-optimally oriented faults become seismically active either because of lower friction coefficients or the presence of fluid pressures in excess of hydrostatic[8–11].

A geologic cross-section integrating surface geology with seismic reflection profiles[12,13] (Fig. 1b) shows that the first two mainshocks nucleated in the Triassic evaporites (made up of alternating anhydrites and dolomites). All earthquakes of moment magnitude $M_w > 5$ nucleated in the evaporites, the same lithologic unit where CO_2 at near-lithostatic pressure was encountered in the San Donato borehole at a depth of 4.8 km about 50 km northwest of Colfiorito[4]. The tectonic environment of the Northern Apennines is suitable for trapping high-pressure fluids derived from CO_2 mantle degassing[14,15], and in particular, the Rasiglia spring in the epicentral region shows an area-averaged deep CO_2 production rate[12] of approximately 6×10^5 mol m^{-2} yr^{-1}.

We show that the driving mechanism for this earthquake and aftershock sequence is the coseismic release and propagation of the trapped high-pressure source into the overlying carbonates at hydrostatic pore pressure. Coseismic fracturing of the seal separating these two distinct pressure states initiates the rapid propagation of a pressure pulse along the newly formed, highly permeable fault zone and into the adjacent damage zone. The newly fractured crust provides high-permeability channels to propagate the pulse and trigger seismicity by significantly reducing the effective normal stress acting on incipient slip planes. In addition, the earthquakes and aftershocks themselves create new fractures, resulting in a large-scale permeability structure that increases significantly as the sequence evolves. This is shown by recasting the epicentres (Fig. 1a) as the approximate slipped area of the sequence (Fig. 2a), demonstrating how the entire region evolves to a complex system of fractures that provide conduits for propagating the pressure pulse.

There are two regions of interest for this study. The first is the largest event of the entire sequence (event 3), and its associated

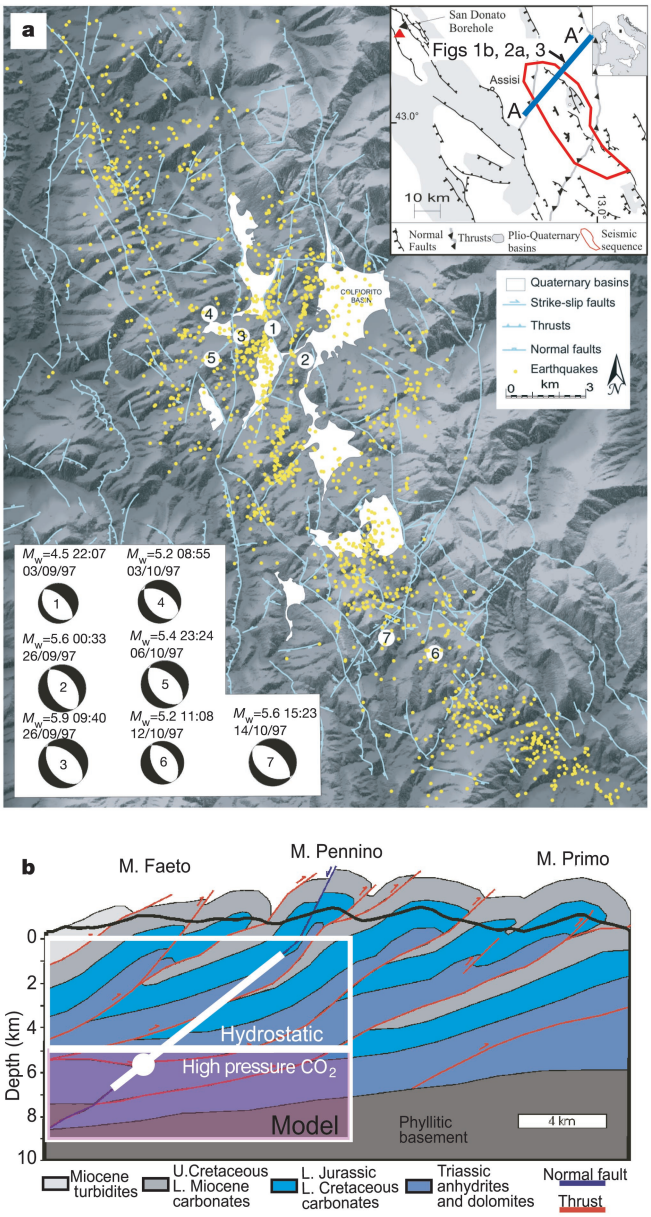

Figure 1 Geologic setting of the study area. **a**, Seismicity and major structures of the Colfiorito region of the Northern Apennines, Italy. The region consists of a complex pattern of thrusts, folds and normal faults reflecting two main tectonic phases: a Miocene–Pliocene compressional phase forming east-northeast (ENE)–verging thrusts and folds; and a superimposed upper Pliocene–Quaternary extensional phase forming basins bounded by NNW–SSE-trending normal faults[12,13]. Near-lithostatic pore pressure (CO_2) measured in the San Donato borehole (see inset) was encountered in the evaporates and just below the seal of a sub-horizontal thrust. All $M_w > 5$ earthquakes nucleated in the evaporates. **b**, Geologic cross-section calibrated from geology and seismic profiles[13], with the simplified model shown superposed (see also Fig. 3). U., Upper; L., Lower.

aftershocks (Fig. 2a). We can approximate and model this sequence by projecting the aftershocks onto a two-dimensional profile (A–A′) that also corresponds to the geologic cross-section in Fig. 1b. The second region of interest is the sequence propagating to the SSE, where the observed propagation velocity (Fig. 2b) can be used to estimate the structural permeability of the system, and to show supporting evidence for the high permeability used in the model. Figure 2b shows that this sequence propagated at a relatively constant velocity of about 1 km d^{-1}, similar to the velocity of CO_2-driven seismicity inferred from a swarm system[16], and for induced seismicity in a deep borehole[17]. A fluid-pressure-induced sequence with a constant propagation velocity is consistent with the wave-like solutions of a pressure pulse found for flow problems where permeability is a strong nonlinear function of the effective normal stress $\bar{\sigma}_n$ acting on the fracture[18,19]. Assuming that the observed propagation velocity reflects the velocity of a wave-like pulse, we can roughly estimate the large-scale permeability of the system using the relationship[18] $V = k\gamma/(n\phi)$, where V is the pulse velocity, k is the intrinsic permeability, γ is the weight density difference between the rock and fluid, η is the viscosity, and ϕ is the porosity. Taking $\gamma = 1.7$ MPa m^{-1}, $\eta = 10^{-3}$ Pa s, $\phi = 0.05$, and using the observed V, then $k = 4 \times 10^{-11}$ m^2. This is a very large permeability compared to the 10^{-16} m^2 inferred for crustal permeability in tectonically stable environments[20], but lower than the permeability inferred for the Dobi extensional earthquake sequence in Central Afar[21], and consistent with permeability measurements on rough fractures in granite and marble at low effective normal stress[22].

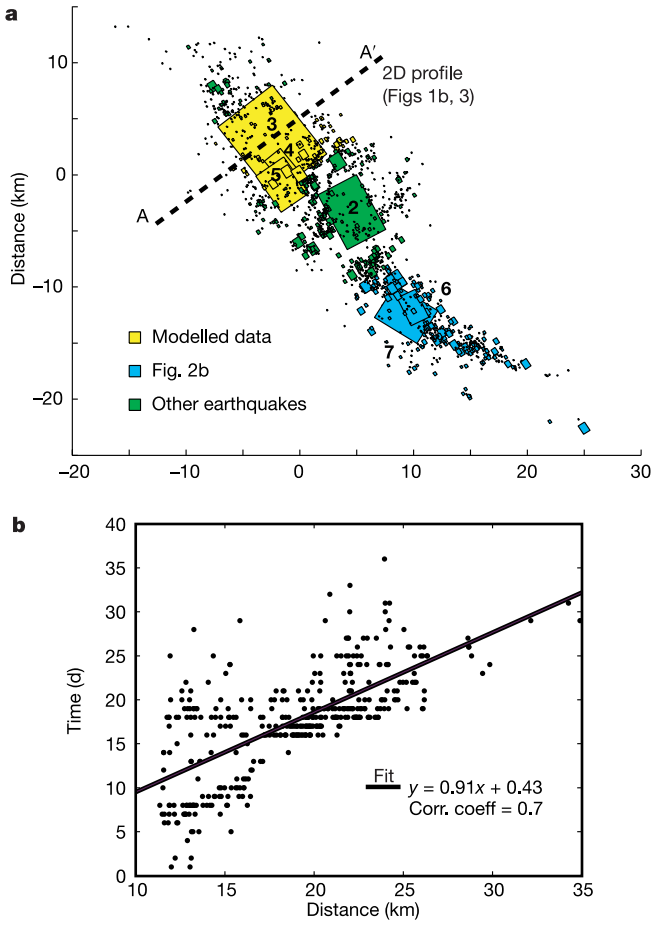

Figure 2 Map view of the seismicity and the rate of propagation. **a**, The seismicity in Fig. 1a recast as the approximate area fractured in the earthquake or aftershock to illustrate how the earthquake or aftershock themselves drastically alter the structural permeability of the system. Patches show the slipped area using the relation $M = GA\bar{u}$, where M is the scalar seismic moment, G is the shear modulus (30 GPa), $\Delta\sigma$ is the stress drop (assumed to be 1.5 MPa), and slip $\bar{u}$ is calculated from $\Delta\sigma = (2G/\pi)(\bar{u}/W)$. The events are colour-coded to show the events (yellow) compared to the model results, and include all events with $M_w > 2.4$ between the hypocentre of event 3 and about 7 km to the NW. Section A–A′ corresponds to the cross-section in Fig. 1b, and represents an approximate two-dimensional profile onto which the hypocentres of events shown in yellow are projected. Events shown in blue are plotted in **b** as the distance from the hypocentre of event 3 versus time to estimate the structural permeability of the system. It is the length of the vector between hypocentres, and therefore includes both the horizontal and up-dip migration of the sequence. The linear correlation implies that the propagation velocity is faster than the $t^{1/2}$ diffusion timescale, and a least-squares fit shows that this sequence propagates at ~1 km d^{-1} (that is, ~10^{-2} m s^{-1}).

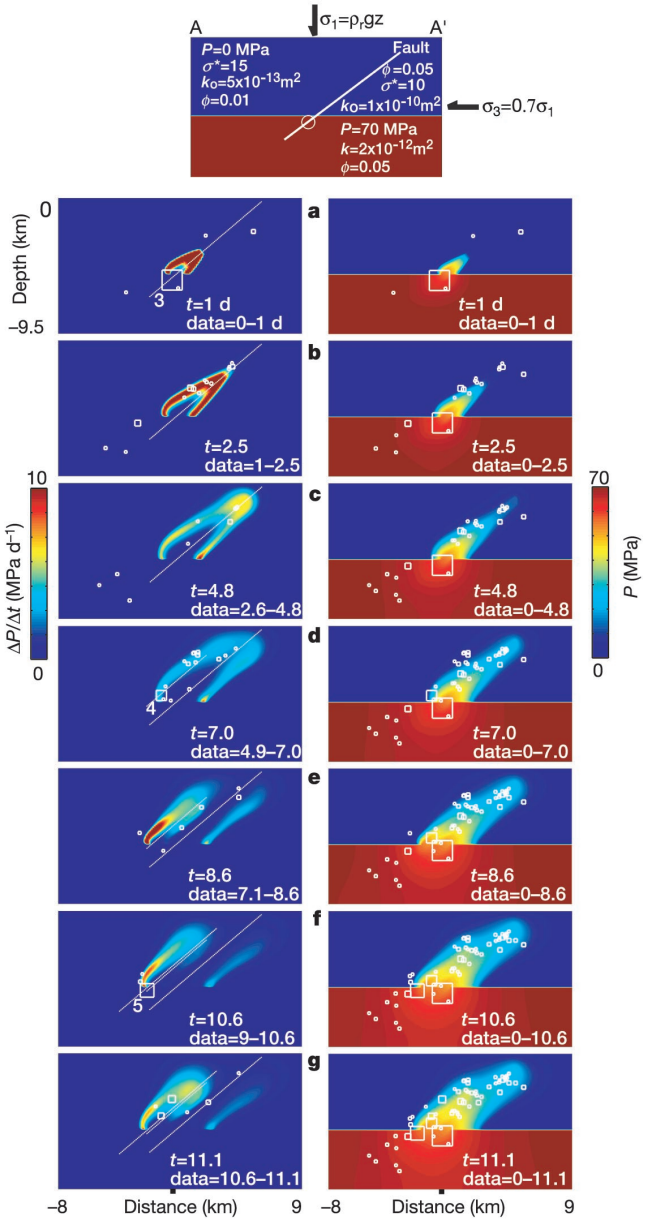

Figure 3 Comparison of model results with initial conditions (top) to the hypocentres of aftershocks (bottom) shown in yellow in Fig. 2a. **a**–**g**, Model results plotted as the rate of pore pressure increase to highlight propagation of the pressure front (left column), and the corresponding evolution of the entire fluid pressure field (right column). The left column compares the evolution of the pore pressure front to the aftershocks occurring during the times indicated. The overall fluid pressure field is superposed with the cumulative aftershock catalogue. The largest event in the sequence (event 3) and subsequent large aftershocks in the hanging wall (events 4 and 5) are indicated in **a**, **c** and **e**.

Modelling the three-dimensional flow field is beyond the scope of this Letter, but we can simplify the analysis by considering the two-dimensional profile perpendicular to the strike of event 3. All aftershocks with $M_w > 2.4$ in the volume surrounding event 3 are projected onto the two-dimensional profile (A–A′) for comparison with model results. We model this sequence by numerically solving a nonlinear diffusion equation with an effective-stress-dependent permeability (see Methods). In the initial conditions, an impermeable seal separates the upper region at hydrostatic fluid pressure from the high-pressure source region where the initial fluid pressure was taken at 85% of lithostatic[4] (for example, 70 MPa) at the upper boundary of the source region. A hydrostatic pressure gradient is imposed below the seal, corresponding to no-flow conditions before the earthquake. Flow initiates at $t = 0$, when a model fault and damage zone approximately 400 m in width (field observations show damage zones from 200 to 600 m) cuts the high-pressure region and extends to about 1 km below the surface. This simulates the coseismic fracturing of the pore pressure seal. The sudden communication between the high-pressure source and low-pressure surroundings initiates a pressure pulse that propagates along the fault and into the hanging and footwalls.

The evolution of the propagating pressure front and the fluid pressure field (Fig. 3) are superposed with the hypocentres of aftershocks for the period indicated in each panel. The steep front is a consequence of the wave-like solution for pressure-dependent permeability, in contrast to a more diffuse front resulting from linear diffusion. At early times (Fig. 3a, b), the pulse propagates rapidly up the fault zone, leaving in its wake a slower-moving pulse into the matrix material of the hanging and footwalls. The faster propagation into the hanging wall relative to the footwall is a result of the decreasing σ_n (thus increasing permeability) as the pulse propagates to shallower depths. As the pulse reaches the hydrostatic boundary condition imposed at the surface, the pressure is reduced but the pulse continues to propagate. The high-pressure front arrives and triggers event 4 (Fig. 3d), which we model by introducing a second fault (with the same properties as the original fault) extending into the source region (dotted line). Because this new high-permeability fault extends into the source region, the system is recharged and generates additional aftershocks (Fig. 3e). The subsequent pulse propagates to the location of event 5 (Fig. 3f), triggering additional seismicity (Fig. 3g). Aftershocks for events 4 and 5 correlate with the rapid propagation of a pulse into the already highly pressurized footwalls of these events.

The evolution of the total fluid pressure in the system (right column of Fig. 3) shows that the data are matched in space and through time, and follow the structure of the evolving fluid pressure field. The aftershocks in the high-pressure source region appear to correlate with contours of reduced fluid pressure. In this case, the mechanism of triggering is probably the transition from aseismic slip at high pore pressures to seismic slip as fluid pressure is reduced[23], or alternatively, a complex source region.

Our model presents an alternative interpretation of the physical processes controlling earthquake triggering in the neighbourhood of the causative fault. Several studies have shown correlations with stressing rate changes[6,24], static stress transfer[1], or poro-elastic effects[25,26]. These models rely on extremely small stress changes (~0.1 MPa) and therefore have not unequivocally demonstrated that simple static stress changes or poro-elastic effects are the dominant mechanism of earthquake triggering or driving aftershocks. The change in Coulomb failure stress (ΔCFS) is defined as $\Delta CFS = \Delta\tau + \mu(\Delta\sigma_n + \Delta P_f)$, where $\Delta\tau$ and $\Delta\sigma_n$ are the shear and normal stress changes (positive in extension), and ΔP_f is the change in pore pressure. Attempts to relate this earthquake sequence to ΔCFS from shear stress changes failed to explain this sequence[2], particularly for the persistence of aftershocks in the hanging wall[3]. Figure 4a shows the aftershock data with the ΔCFS (for stress changes only) for event 3, and Fig. 4b compares the same aftershock data with the calculated pressure field.

In most ΔCFS formulations, the focus is primarily on changes in τ and σ_n, and it was found to be difficult to properly include poro-elastic effects[27]. For event 3, ΔCFS from shear and normal stress changes are on the order of a few tenths of an MPa. Significantly, our results show that the effect from a 10–20 MPa direct fluid pressure loading (for example, ΔP_f) overwhelms static stress transfer.

The structural, seismic and post-seismic response of this sequence support a scenario where high-pressure CO_2 infiltrated the incipient seismic fault before the large earthquakes, followed by a large-scale change in the hydraulic properties of the system. The coseismic fracture generated a high-amplitude pressure pulse initiating at the high-pressure/low-pressure boundary, propagating into the damaged region caused by the mainshock. The increased fluid pressure triggered subsequent earthquakes and aftershocks by significantly reducing the effective normal stress. The results also suggest that the aftershocks in regions of increasing pore pressure occur along contours of constant $\bar{\sigma}_n$, implying that earthquakes occurred at the same shear stress (assuming a constant friction coefficient) independently of depth. As the effect on ΔCFS due only to pore pressure changes is orders of magnitude greater than the contribution of elastic stress transfer, we propose that this mechanism dominates some triggering phenomena and aftershock sequences. Although this sequence was driven by CO_2 out-gassing, the processes of fracture and coseismic hydraulic property changes are general, suggesting this is an important general mechanism of aftershock generation. That is, earthquakes provide the trigger to hydraulically connect the upper crust at hydrostatic pore pressure with the lower crust at near-lithostatic pore pressure. The subsequent flow will be fast, high-pressured, and will propagate readily into the new fractures created by the main event. □

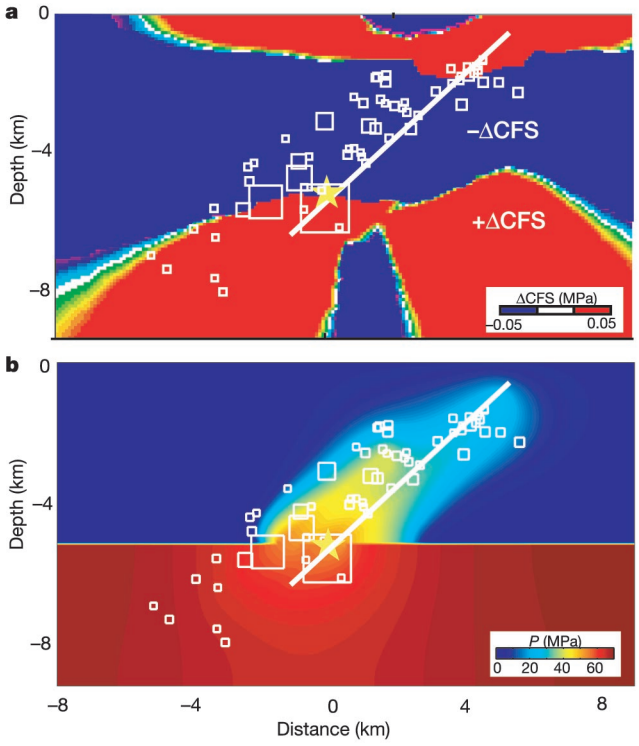

Figure 4 Comparison of aftershock data to stress changes in the ΔCFS formulation and pore pressure changes. **a**, There is no correlation between positive or negative ΔCFS regions and the aftershock locations. In contrast, **b**, the same aftershock data compared to the calculated fluid pressure state after 11 days, shows a very strong correlation with the entire aftershock sequence (see also Fig. 3.)

Methods

We adopt the model of Rice[18] where permeability is a strongly decreasing function of effective normal stress, $k = f(\bar{\sigma}_n)$. Specifically, $k = k_0 \exp(-\bar{\sigma}_n/\sigma^\star)$, where k_0 is the permeability at zero effective stress, and $\sigma^\star$ is a constant with lower values of $\sigma^\star$ corresponding to highly cracked rocks. Using this form for the permeability, we solve the diffusion equation with a spatially variable permeability[28]:

$$\frac{\partial P}{\partial t} = \frac{1}{\phi(\beta_f + \beta_\phi)}\left[\nabla \frac{k_0 \exp\left(-\frac{\bar{\sigma}_n}{\sigma^\star}\right)}{\eta} \nabla P + \dot{\Gamma}(P,T)\right] \quad (1)$$

where P is the fluid pressure above hydrostatic, β_f and β_ϕ are the fluid and pore (crack) compressibility, and $\dot{\Gamma}$ is a source term. The source term is assumed to be zero here, but is included in equation (1) to show that the pressure dependence of the dehydration (or de-carbonization) kinetics could provide an additional direct fluid source from coseismic fluid pressure reductions[29]. The effective normal stress used in equation (1) and acting on fault planes is calculated as[30]:

$$\bar{\sigma}_n = \frac{\sigma_1 + \sigma_3 - 2P_f}{2} + \frac{\sigma_1 - \sigma_3}{2}\cos 2\theta \quad (2)$$

where σ_1 and σ_3 are the maximum and minimum principal stress, P_f is the total fluid pressure (for example, $P + \rho_w g z$), θ is the dip angle, ρ_w is the density of water, g is the acceleration of gravity, and z is the depth. We take $\theta = 40°$ (determined from the earthquake focal mechanisms), σ_1 as the weight of the overburden (for example, $\rho_r g z$), where ρ_r is the rock density, and we assume $\sigma_3 = 0.7\sigma_1$ to reflect this extension tectonic environment.

We solve equation (1) with an implicit finite difference scheme, using the simplified model geometry and initial conditions shown at the top of Fig. 3. A no-flow boundary condition is imposed on all boundaries except the upper surface, where a constant head (for example, hydrostatic pore pressure) boundary condition is imposed. We use crack compressibility $\beta_\phi = 10^{-8}\,\mathrm{MPa}^{-1}$, fluid compressibility $\beta_f = 10^{-10}\,\mathrm{MPa}^{-1}$, and a temperature-dependent viscosity for water (assuming a temperature gradient of $25\,°\mathrm{C\,km}^{-1}$). We assume that the flow properties of supercritical CO_2 (the phase of CO_2 at the source depth) are the same as for water because CO_2 at this P–T condition is ten times more compressible than water, but it is of the same order less viscous, resulting in similar flow properties. Note that the model can be made much more complicated by considering two-phase flow, dual porosity, anisotropic permeability, and other complexities. However, we find this simple model sufficient to show a very strong correlation between the calculated pressure field and the precise locations of aftershock hypocentres.

Received 13 June; accepted 25 November 2003; doi:10.1038/nature02251.

1. Stein, R. S. The role of stress transfer in earthquake triggering. *Nature* **402,** 605–609 (1999).
2. Cocco, M., Nostro, C. & Ekstrom, G. Static stress changes and fault interaction during the 1997 Umbria-Marche earthquake sequence. *J. Seismol.* **4,** 501–516 (2000).
3. Chiaraluce, L., Ellsworth, W. L., Chiarabba, C. & Cocco, M. Imaging the complexity of an active normal fault system; the 1997 Colfiorito Central Italy case study. *J. Geophys. Res. B* **6,** 10.1029/2002JB002166 (2003).
4. Chiodini, R. & Cioni, G. Gas geobarometry for hydrothermal systems and its application to various Italian geothermal areas. *Appl. Geochem.* **4,** 564–572 (1989).
5. Waldhauser, F. & Ellsworth, W. L. A double-difference earthquake location algorithm: Method and application to the Northern Hayward Fault, California. *Bull. Seismol. Soc. Am.* **90,** 1353–1368 (2000).
6. Toda, S., Stein, R. & Saglya, T. Evidence from the AD 2000 Izu islands earthquake swarm that stressing rate governs seismicity. *Nature* **419,** 58–61 (2002).
7. Collettini, C. Structural permeability control on the post-seismic fluid discharge and aftershocks triggering; hypotheses for the 1997 Colfiorito earthquakes. *Boll. Soc. Geol. It.* **1,** 873–880 (2002).
8. Sibson, R. H. Fault-valve behavior and the hydrostatic-lithostatic fluid pressure interface. *Earth Sci. Rev.* **32,** 141–144 (1992).
9. Cox, S. F. Faulting processes at high fluid pressures: An example of fault valve behavior from the Wattle Gully Fault, Victoria, Australia. *J. Geophys. Res.* **100,** 12841–12859 (1995).
10. Miller, S. A., Nur, A. & Olgaard, D. L. Earthquakes as a coupled shear stress-high pore pressure dynamical system. *Geophys. Res. Lett.* **23,** 197–200 (1996).
11. Streit, J. E. & Cox, S. F. Fluid pressures at hypocenters of moderate to large earthquakes. *J. Geophys. Res.* **106,** 2235–2243 (2001).
12. Reuter, K. J., Giese, P. & Closs, H. Lithosphere split in the descending plate; observations from the Northern Apennines. *Tectonophysics* **64,** T1–T9 (1980).
13. Mirabella, F. & Pucci, S. Integration of geological and geophysical data along two sections crossing the region of the 1997–98 Umbria-Marche earthquake sequence. *Boll. Soc. Geol. It.* **1,** 891–900 (2002).
14. Chiodini, G., Frondini, F., Cardellini, C., Parello, F. & Peruzzi, L. Rate of diffuse carbon dioxide Earth degassing estimated from carbon balance of regional aquifers: The case of central Apennine, Italy. *J. Geophys. Res.* **105,** 8423–8434 (2000).
15. Quattrocchi, F. In search of evidence of deep fluid discharges and pore pressure evolution in the crust to explain the seismicity style of the Umbria-Marche, 1997–1998 seismic sequence (Central Italy). *Ann. Geophys.* **42,** 609–636 (1999).
16. Bräuer, K., Kämpf, H., Strauch, G. & Weise, S. M. Isotopic evidence ($^3He/^4He$, $^{13}C_{CO_2}$) of fluid-triggered intraplate seismicity. *J. Geophys. Res.* **108,** 10.1029/2002JB002077 (2003).
17. Baisch, S. & Harjes, H.-P. A model for fluid-injection-induced seismicity at the KTB, Germany. *Geophys. J. Int.* **152,** 160–170 (2003).
18. Rice, J. R. in *Fault Mechanics and Transport Properties of Rock* (eds Evans, B. & Wong, T.-f.) 476–503 (Academic, San Diego, 1992).
19. Revil, A. & Cathles, L. M. III Fluid transport by solitary waves along growing faults. A field example from the South Eugene Island Basin, Gulf of Mexico. *Earth Planet. Sci. Lett.* **202,** 321–335 (2002).
20. Manning, C. E. & Ingebritsen, S. E. Permeability of the continental crust: Implications of geothermal data and metamorphic systems. *Rev. Geophys.* **37,** 127–150 (1999).
21. Noir, J., Jacques, E., Bèkri, S., Adler, P. M. & King, G. C. P. Fluid flow triggered migration of events in the 1989 Dobi earthquake sequence of Central Afar. *Geophys. Res. Lett.* **24,** 2335–2338 (1997).
22. Lee, H. S. & Cho, T. F. Hydraulic characteristics of rough fractures in linear flow under normal and shear load. *Rock Mech. Rock Eng.* **35,** 299–318 (2002).
23. Segall, P. & Rice, J. R. Dilatancy, compaction, and slip instability of a fluid infiltrated fault. *J. Geophys. Res.* **100,** 22155–22171 (1995).
24. Dieterich, J. A constitutive law for rate of earthquake production and its application to earthquake clustering. *J. Geophys. Res.* **99,** 2601–2618 (1994).
25. Nur, A. & Booker, J. R. Aftershocks caused by pore fluid flow? *Science* **175,** 885–887 (1972).
26. Bosl, W. J. & Nur, A. Aftershocks and pore fluid diffusion following the 1992 Landers earthquake. *J. Geophys. Res.* **107,** 10.1029/2001JB000155 (2002).
27. Cocco, M. & Rice, J. R. Pore pressure and poroelasticity in Coulomb analysis of earthquake interactions. *J. Geophys. Res.* **107,** 10.1029/2000JB000138 (2002); correction 10.1029/2002JB002319 (2003).
28. Wong, T.-f., Ko, S.-c. & Olgaard, D. L. Generation and maintenance of pore pressure excess in a dehydrating system, 2, Theoretical analysis. *J. Geophys. Res.* **102,** 841–852 (1997).
29. Miller, S. A., van der Zee, W., Olgaard, D. L. & Connolly, J. A. D. A fluid-pressure controlled feedback model of dehydration reactions: Experiments, modelling, and application to subduction zones. *Tectonophysics* **370,** 241–251 (2003).
30. Jaeger, J. C. & Cook, N. G. W. *Rock Mechanics* (Chapman and Hall, London, 1979).

Acknowledgements We thank C. H. Scholz for comments, and D. Giardini, Y. Y. Podladchikov, J. A. D. Connolly, T. Kohl, K. Evans, G. Hillers and N. Deichmann for discussions.

Authors' contributions C.C., structural geology and concept development; L.C. and M.C., aftershock data; M.B., structural geology; B.J.P.K., numerical model development.

Competing interests statement The authors declare that they have no competing financial interests.

Correspondence and requests for materials should be addressed to S.A.M. (steve.miller@erdw.ethz.ch).

Changes in fisheries discard rates and seabird communities

Stephen C. Votier[1], Robert W. Furness[1], Stuart Bearhop[1,2], Jonathan E. Crane[1], Richard W. G. Caldow[3], Paulo Catry[4], Kenny Ensor[1], Keith C. Hamer[5], Anne V. Hudson[1], Ellen Kalmbach[6], Nicholas I. Klomp[7], Simone Pfeiffer[1,8], Richard A. Phillips[9], Isabel Prieto[1] & David R. Thompson[10]

[1]*Institute of Biomedical and Life Sciences, University of Glasgow, Glasgow G12 8QQ, UK*
[2]*School of Biology and Biochemistry, Queens University, Belfast, Medical Biology Centre, 97 Lisburn Road, Belfast BT9 7BL, UK*
[3]*Centre for Ecology and Hydrology, Winfrith Technology Centre, Winfrith Newburgh, Dorchester, Dorset DT2 8ZD, UK*
[4]*Unidade de Investigação em Eco-Etologia, ISPA, Rua Jardim do Tabaco 44, Lisboa, Portugal*
[5]*Faculty of Biological Sciences, University of Leeds, Leeds LS2 9JT, UK*
[6]*Department of Animal Ecology, University of Groningen, Kerklaan 30, 9751NN Haren, The Netherlands*
[7]*Johnstone Centre, School of Environmental and Information Sciences, Charles Sturt University, PO Box 789, Albury, New South Wales 2640, Australia*
[8]*Institute of Ecology, Dornburger Strasse 159, University of Jena, 07743 Jena, Germany*
[9]*British Antarctic Survey, High Cross, Madingley Road, Cambridge CB3 0ET, UK*
[10]*National Institute of Water and Atmospheric Research Ltd, PO Box 14-901, Kilbirnie, Wellington, New Zealand*

It is clear that discards from commercial fisheries are a key food resource for many seabird species around the world[1–8]. But predicting the response of seabird communities to changes in discard rates is problematic and requires historical data to elucidate the confounding effects of other, more 'natural' ecological processes. In the North Sea, declining stocks, changes in technical measures, changes in population structure[9] and the establishment of a recovery programme for cod (*Gadus morhua*[10]) will alter the amount of fish discarded. This region also supports internationally important populations of seabirds[11], some of which feed extensively, but facultatively, on discards, in particular on undersized haddock (*Melanogrammus aeglefinus*)